Multisensor Localization Architecture for High-Accuracy and High-Integrity Land-based Applications

Omar García Crespillo, Anja Grosch, Patrick H. Adjroloh, Chen Zhu *German Aerospace Center*
Roberto Capua, Fabio Frittella *Sogei*
Ondrej Kutik *Roboauto*

BIOGRAPHY

Omar García Crespillo is the leader of the Integrated Navigation Systems Integrity group at the Navigation department of the German Aerospace Center (DLR). He holds a PhD from the Swiss Federal Institute of Technology (EPFL), 2022 and a M.Sc. in Telecommunication Engineering from the University of Malaga in Spain, 2013. His current field of research includes ARAIM and integrity monitoring in GNSS/INS and high accuracy GNSS for safe ground and air transportation systems

Anja Grosch received the German diploma in Computer Engineering from the Ilmenau University of Technology, Germany in 2007. After her graduation, she worked for the communications department on channel coding, OFDM systems and relay networks. Since March 2008, she has joined the Institute of Communications and Navigation of the German Aerospace Center. Her main focus has been multisensor fusion algorithms, especially GNSS and INS integration. She develops integrity concepts of these integrated systems optimized for different safety-of-life applications.

Patrick H. Adjroloh obtained his Master's degree in Aerospace Systems, Navigation and Telecommunications from the Ecole Nationale de l'Aviation Civile (ENAC), France in 2019. After graduation, he worked on GNSS signals processing in projects related to the European SBAS system EGNOS. He joined the department of Navigation of the institute of Communications and Navigation in the German Aerospace Center since October 2020. His research interest lies in multisensor integration with particular focus on GNSS and inertial sensors.

Chen Zhu is a senior research fellow and the head of Visual and Terrestrial Augmentation group at the Institute of Communications and Navigation, German Aerospace Center (DLR). He received his Ph.D. degree (Dr.-Ing.) and Master's degree (M.Sc.) from Technical University of Munich, Germany and his Bachelor's degree from Tsinghua University, Beijing, China. His research fields include visual navigation, multisensor fusion, UAS and robotic swarm navigation, currently focusing on the system integrity.

Roberto Capua received a Master Degree in Electronic Engineer. He has multidecennal experience in GNSS applications and R&D for Public and Private Organisations. He worked in the aerospace industry for EU Programmes on Galileo design and application developments. His areas of activity include high precision GNSS, Software Receiver, navigation and communication systems for Road, Rail, Inland waterway, Aerospace and Surveying. He is currently responsible for GNSS R&D for Sogei, secretary of the Space Y association and Chairman of the RTCM SC-134 Committee.

Fabio Frittella has a Master Degree in Electronic Engineering, with consolidated background in Electronic design field and software development. He worked also on data network design and middleware infrastructures for multimedia applications for public organization. He widened his areas of activities working on GNSS network control center and developing standards communication protocols for GNSS applications. He participated to design of GNSS SDR hardware. He is collaborating within Horizon 2020 projects ERSAT EAV, ERTMS on Satellite – Enabling Application Validation and RHINOS Railway High Integrity Navigation Overlay System. Currently he is working in Sogei GNSS R&D group.

Ondrej Kutik obtained Master's degree in Wireless Systems at the Royal Institute of Technology, Sweden in 2004. Since then he works in positioning related disciplines for the industry sector. Starting his career as R&D engineer for digital signal processing, including design of airborne GNSS receiver. Currently acts as a product manager for innovative positioning technologies.

ABSTRACT

Emerging safety-related applications like autonomous vehicles will require high levels of navigation performance in terms of accuracy while still satisfying stringent requirements of integrity, availability and continuity. Achieving sub-meter accuracy in land-based scenarios with GNSS-based solutions can only be achieved with carrier-phase based approaches in combination with additional sensors. So that these solutions can be considered for future certified systems, the safety aspect must be ensured, which is still a challenge in the presence of local GNSS threats (like multipath or NLOS) as well as in multisensor architectures. In this work, we propose a multisensor architecture that uses float Real-Time Kinematic (RTK) GNSS with additional integrity information from an augmentation network. The architecture also considers different layers of protection against local GNSS threats that supports the rigorous design of integrity monitoring algorithms and protection level computation. GNSS is combined with additional sensors like Inertial Measurement Unit (IMU) and a robust relative location of the vehicle is complemented with stereo camera and vision processing. This allows for different possible types of localization modes. The algorithms are validated with real measurements collected with a car during a measurement in Rome, Italy. The results show clearly that our design can achieve high accuracy while ensuring high integrity.

I. INTRODUCTION

Different Intelligent Transportation Systems (ITS) and new emerging autonomous land-based applications require of a precise-accurate positioning information that can be trusted. According to the European Union Agency for the Space Programme (EUSPA) (formely GSA) consultation reports (GSA, 2019a,c,b), the requirements for these applications can reach submeter accuracy and stringent alert limits with low integrity risk. Even though high integrity GNSS positioning can offer a reliable solution for civil aviation applications and is continuously evolving, the environment on land presents a lot of challenges to guarantee a certain integrity level as well as the availability of the positioning system based solely on GNSS. In order to provide high-accurate, high-integrity solutions, it is widely agreed that multiple sensor fusion technologies are necessary. However, the combination of multiple sensors poses on its own new problems so that the integrity of the system can be demonstrated. In particular, the following expected challenges and foreseen solutions are considered when designing a safe localization architecture:

- Use of augmentation messages for high accuracy and high integrity GNSS measurements
- Adoption of suitable detectors to protection against the presence of local GNSS threats such as multipath, NLOS and interferences
- Rapid changing number of visible satellites due to urban environment
- Trustable and error bounded integration of different sensor technologies
- Coasting capability during periods of no satellite visibility to ensure the provision of a continuous solution
- Adaptability to sensor quality information

Previous work has addressed the provision of GNSS integrity in urban environments Zhu et al. (2018), also in combination with other sensors Saidani et al. (2021); Meng and Hsu (2021); Toledo-Moreo et al. (2007); Bijjahalli and Sabatini (2021). However, in many cases, no high accuracy solutions are taken into account or integrity algorithms used in the aviation domain (like RAIM or SBAS) are proposed without rigorous consideration of the differences in the operational environment Joerger and Spenko (2017), like error models, probabilities of faults or bounding of estimation errors with different estimators than least-squares.

In this work, we propose an architecture that uses multifrequency-multiconstellation GNSS in Real Time Kinematic with additional integrity augmentation information, Inertial Measurement Unit (IMU) and stereo cameras. Additional layers of protection are added against local threats, which allows for a more rigorous assumption about residual fault probabilities and protection level derivation. A localization mode selector is also included as an interface to the user to increase the availability of solutions even if in a degraded mode of operation.

The algorithms performance, methodology and behavior of the multisensor system is evaluated with real measurements in automotive environment recorded during a demonstration campaign of the European H2020 project HELMET. The architecture proposed and the different processing blocks considered in this work address several of the aspects so that an accurate and high-integrity positioning information can be provided for land-based applications. The results validate the benefit of the different fault detection and error protections and the possibility to provide protection levels in RTK float type solutions. This solution may not only be considered as a baseline for automotive but for other land-based or close to ground navigation in non-restricted environments (e.g., railways or UAVs).

II. REQUIREMENTS AND HIGH LEVEL SYSTEM CONCEPT

The demand on safety-related navigation solution with very stringent requirements on accuracy, integrity as well as availability and continuity has been constantly increasing in the last years. To provide an overview, we have summarized the joint requirements of different applications in terms accuracy and integrity in Figure 1. This diagram is based on the different EUSPA requirements reports on user requirements for road, rail and UAV (GSA, 2019a,b,c). On the x-axis you can see the required Alert Limits in meters and on the y-axis the target Integrity risk. As a comparison you can find the requirements of different operations in civil aviation in the lower right area with red squares. The orange triangles depict different railway operations. The green line identifies the potential requirements of UAV operations and the two blue lines with diamonds are representing the requirements of two potential automotive applications. For automotive, a parallel study with somehow similar requirements is Reid et al. (2019). In contrast to civil aviation, the requested accuracy performance are up to two order of magnitudes more stringent, whereas the allowed integrity risk might be significantly smaller depending on the application and requested operation but it is also comparable for the most critical applications. This sets a new scenario where to meet the accuracy requirements, the usage of carrier-phase based GNSS processing options (compared to only code-based) in combination with additional other sensors is mandatory. Another huge difference to the well-elaborated civil aviation, is the local propagation environment of the satellite signals. The potential presence of multipath, non-line of sight reception, interference, jamming or even spoofing is much larger and hence, it need to be treated differently since the operational environment is not apriori restricted (like for instance an airport).

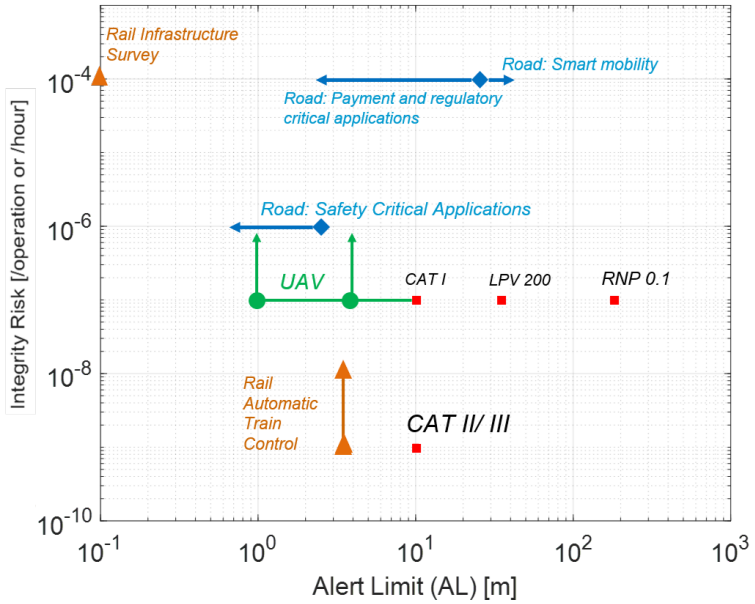

Figure 1: Alert limit and integrity risk requirements for safety/liability related applications (GSA, 2019a,b,c)

III. THE AUGMENTATION SYSTEM AND BASE STATIONS FOR VALIDATION

For the Pilot Development, an Augmentation System for High Accuracy and Integrity Augmentation has been developed, starting from the existing Sogei GRDNet (GNSS R&D Network) facilities. The Augmentation Integrity Monitoring Network (AIMN) consists of many Reference stations which receive multiconstellation (GPS, GLONASS, Beidou and Galileo) and multifrequency GNSS signals. The Reference Stations have been connected to the Sogei GRDNet Control Center through http. Here, the real-time 2-Tiers FDE algorithms is running and provides RTK messages and experimental Integrity messages, following the SC-134 Experimental Messages 1 and 2 have been developed.

Such messages contains the SIS Integrity Status flags of the Constellation and Reference Stations, leaving the user receiver the responsibility to integrate their autonomous algorithms for local hazard monitoring. The AIMN is based on the analysis of code and phase residuals for developing satellite and Reference Station FDE (Fault Detection and Exclusion). The Augmentation Monitoring System process is shown in Figure 2.

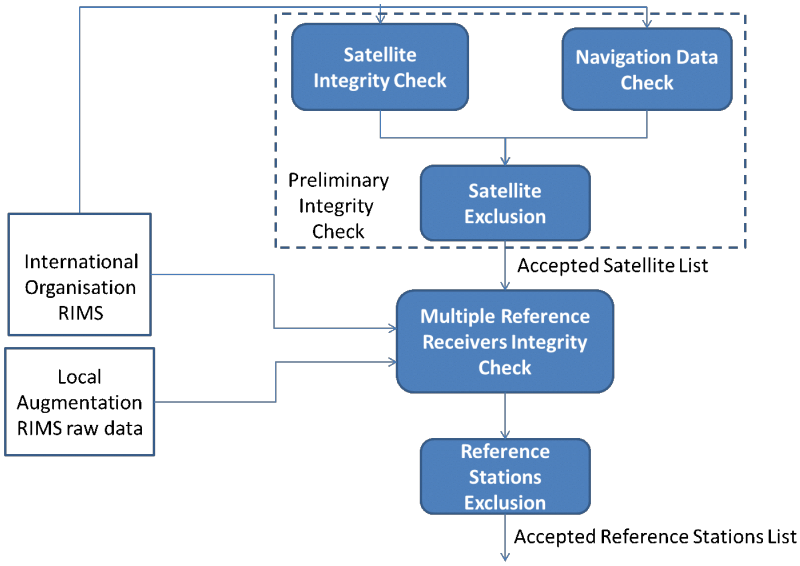

Figure 2: 2-Tiers Algorithm Processing flow

The 2-Tiers algorithm is based on the processing of real-time Reference Station raw measurement between satellite and between receivers difference residuals for both SIS and Reference Station FDE. That is the FDE for satellite exclusion is based on the calculation of Single Differences residuals among satellites and the comparison with a statistical derived threshold (Neri et al., 2015). It is defined as a function of the probability of false alert or probability of missed detection, following the Neyman-Pearson criterion. The test statistic is represented by the weighted squared norm of single differences residuals:

$$\tilde{y}^i_{cod} = [\boldsymbol{\zeta}^i(k)]^T \mathbf{R}^{-1}_{\boldsymbol{\zeta}^i} \boldsymbol{\zeta}^i(k) \tag{1}$$

where $\mathbf{R}_{\boldsymbol{\zeta}^i}$ is the covariance matrix of single differenced measurements and i is the analyzed satellite.
The single difference residual is defined as:

$$\boldsymbol{\zeta}^i(k) = \tilde{\mathbf{S}}^{(i)} \boldsymbol{\Delta\rho}_{Tier2}(k) \tag{2}$$

where $\mathbf{S}$ is the satellite differencing matrix with respect to satellite i.
Following the Neyman-Pearson criterion, fault detection thresholds are set according to the given Missed Exclusion of False Exclusion probabilities. Given the $n-$th Reference Station, for the $i-$th satellite, the algorithm first rearranges the single differences $\{\zeta^{i,j}_n(k), 1 \leq j \leq N_{sat}, j \neq i\}$, where N_{sat} is the number of visible satellites. A fault on the signal related to the $i-$th satellite code channel will affect every $y^j_{cod,n}$. Nevertheless, the contribution to $y^i_{cod,n}$ is $(N_{sat}-1)$ times the contribution to $y^j_{cod,n}$. Thus the signal originating large values can be detected by selecting the satellite corresponding to the largest $y^j_{cod,n}$. A satellite is excluded if the above statistics overcome a defined threshold $\gamma_{y^i_{cod}}$.

The same procedure is applied to the raw phase single differences $\{\mathfrak{I}^{i,j}_n(k), 1 \leq j \leq N_{sat}, j \neq i\}$ rearranged into the vector $\mathfrak{I}^i_n(k)$ in a similar way.

Such an algorithm is carried out iteratively for all single differences for satellite FDE.
The same approach is used for the exclusion of reference stations, where double difference among satellites and reference station are used for calculation and checking. In order to check for reference stations failure, we have to isolate the error contribution introduced into the augmentation by the single reference station.
At this aim, for each reference station, the statistics derived from the double differences residuals with respect to raw data provided by the first tier are calculated:

$$\mathbf{Z}_{cod,n} = [\boldsymbol{\zeta}_{n,Tier1}(k)]^T \tilde{\mathbf{R}}^{-1}_{\boldsymbol{\zeta}_{n,Tier1}} \boldsymbol{\zeta}_{n,Tier1}(k) \tag{3}$$

where

$$\boldsymbol{\zeta}_{n,Tier1}(k) = \mathbf{SD}^{(1)}_{(N_{RIM_1+1})} \boldsymbol{\Delta\rho}_{raw}(k) \tag{4}$$

and $\mathbf{D}$ is the double difference operator. Reference Station from highly reliable reference stations can be used as first tiers (e.g. EGNOS RIMS or EUREF Reference Stations). The algorithm can work also with the second tier only (Local Reference Stations). The probability of excluding the n-th healthy Reference Station while it is healthy is given as a design parameter and it is provided by:

$$P^{RIM}_{FE,z^i_n} = 1 - D_{G_{X^2_{N_Z}}} \left(\gamma_{Z^i_n}; \breve{\Lambda}_{z^i_n} \right) \tag{5}$$

where $\Lambda_{z^i_n}$ is the vector of eigenvalues of $R_{\zeta_{n,Tier1}}$ and

$$D_{G_{X^2_n}}(X;\Lambda) = \frac{1}{\prod_{i=2}^{n} \Lambda_2} D_{X^2_1}\left(\frac{X}{\Lambda_1}\right) * p_{X^2_1}\left(\frac{x}{\Lambda_2}\right) * \cdots * p_{X^2_1}\left(\frac{x}{\Lambda_n}\right) \tag{6}$$

is the cumulative generalized Chi-Square distribution. Given these results, the exclusion threshold can be derived accordingly (Neri et al., 2015).

The output of these FDE algorithms are the Satellite and Reference Stations Integrity Status flags which are passed to the RTK/NRTK Control Centre engine or to the user receiver for relevant resources exclusion. Satellite and Reference Station Integrity Status flag Data Fields and messages have been proposed within SC-134 for integrity monitoring purposes.

IV. ONBOARD SYSTEM ARCHITECTURE AND INTEGRITY MONITORING

This section provides a more detailed architecture and algorithm design of the multisensor on-board unit for the automotive application. It primary considered that at least the available sensors on the vehicle are GNSS, Inertial Measurement Unit (IMU) and a stereo camera system.

The general detailed architecture of the onboard system is shown in Fig. 3, where the onboard unit is divided between the sensing units (GNSS antenna and receiver, Cameras and IMU) and the processing of the physical magnitudes to finally provide the vehicle position and dynamics and related integrity information. The software processing is subdivided in 3 main blocks:

- GNSS Processing channel
- Sensor fusion & Integrity Monitoring Channel
- Camera processing channel

It is additionally considered a preliminary Localization Mode Selector block that makes smart decisions about the most suitable combination of sensors and GNSS augmentation information, and the best solution that must be provided to the user. In the next sections, each of the processing channels are described more in detail.

1. GNSS Processing

The GNSS processing block receives the RF signal from the GNSS Antenna installed on the roof of the vehicle and performs the normal GNSS receiver signal processing to extract the raw measurements (i.e., multifrequency, multiconstellation code and carrier phase). Additionally, in the context of the high-accuracy, high-integrity positioning the following blocks and functions are considered:

a) Local Threats Protection Functions

GNSS Positioning on land-based applications is highly affected by the presence of different local threats that cannot be corrected or compensated for by augmentation information (e.g., EGNOS or the HELMET augmentation subsystem). The protection functions are mainly targeted at detecting the presence of local effects that can corrupt the GNSS code and carrier measurements

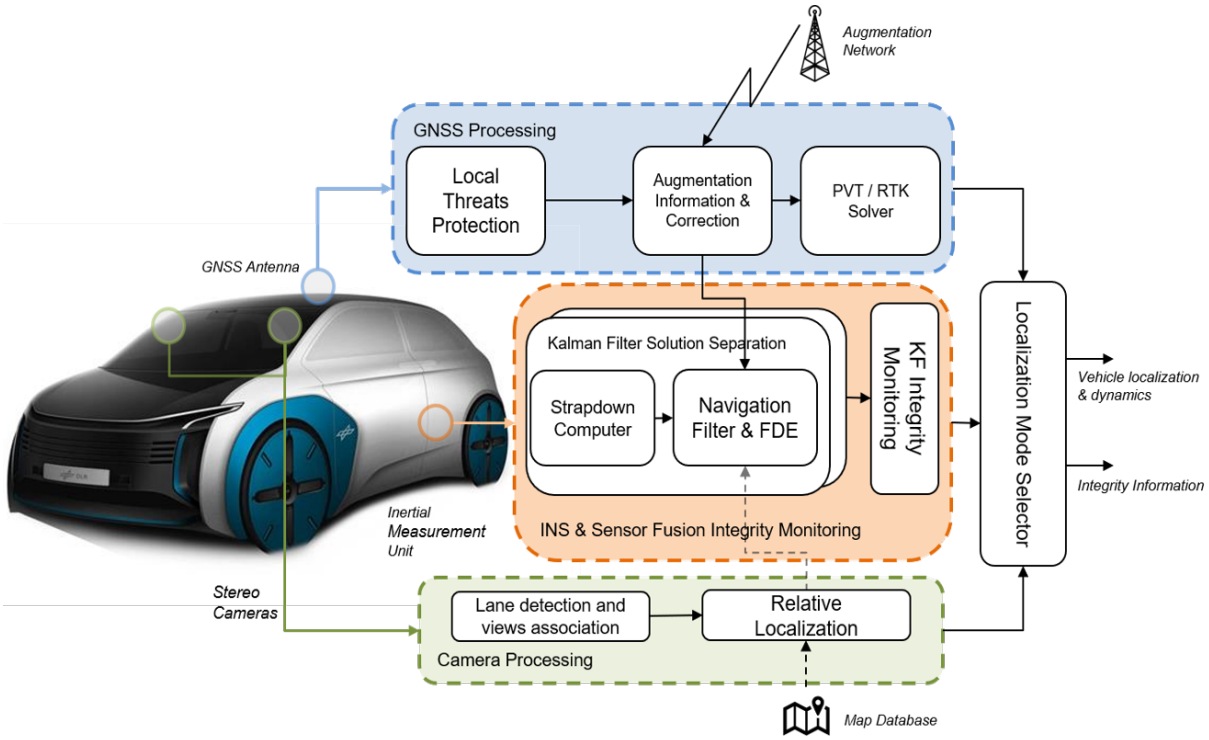

Figure 3: Onboard Multisensor System Architecture

in a way that their error is not representative of the nominal error model that will be considered by the estimation algorithm. A list of relevant local threats and possible detection techniques is provided in (Garcia Crespillo et al., 2019) for land based applications. The following protection measures can be typically at least be considered:

- **RFI detection based on PSD analysis:** Suitable COTS GNSS receivers provide information about the frequency spectrum or can provide the I/Q samples to allow for the computation of it. By comparing a nominal PSD with the current time received one, the presence of different types of narrow/wide band interferences can be detected (Vennarini et al., 2020).
- **Excessive multipath detection:** Based on the Code-minus-Carrier (CMC) observable, a multipath detector can be built for urban scenarios based on the expected rate change of multipath (Caamano et al., 2020). If strong multipath is detected on a certain channel, the corresponding measurements from that satellite are discarded
- **Data editing:** Discarding measurements by applying reasonable checks and decisions has proven to reduce the presence of large unbounded measurement errors (Bryant et al., 2019). Discarding measurements based on this criteria is here called data editing. These measures consider for instance: Applying a certain CN0 mask, discarding measurements based on the loss of lock indicator (LLI), discarding measurements where both L1 and L2 measurements are not available, etc

The excessive protection against local threats may have a big impact on measurements availability. A trade-off must be found between nominal error model and threats protection to satisfy the availability requirement. It is however expected that continuity and availability of the final solution is ensured thanks to the presence of additional sensors, like inertial measurement units and its filter-based coupling. It is therefore important to guarantee the integrity of the measurements even if this reduces the number of available (i.e., trustable) code and carrier phase measurements.

b) Augmentation Information & Correction

Depending on the type of external information that is available and that will determine the main processing channel localization mode, this block may receive:

- The HELMET augmentation information as described in the Section “Augmentation System” (Section 2).
- EGNOS integrity and correction information.
- PPP satellite orbit and clock correction products.

When available this block can:

- Apply the Integrity Status flags to discard those satellites that have been determined unhealthy by the augmentation system.
- Perform corrections to code/phase measurements applying the augmentation data.
- Relay both the onboard measurements and the augmentation information and ground station measurements to allow for a relative baseline estimator and ultimately an absolute position computation based on it.

c) PVT / RTK solver

In certain situations, with enough satellite visibility, it is possible to compute a GNSS-only position, either via SPP, PPP or RTK. This constitutes a possible localization mode that might be available at the vehicle. For instance, RTK (float or fixed solution) can be particularly interesting in static situations and/or to support a fast convergence of other float-based (multisensor) solution.

2. Integrated INS/RTK processing

The INS & Sensor Fusion block is the core positioning block for the automotive application since it is the only one that can guarantee a continuous and high frequency positioning information thanks to the inertial measurement unit that is not affected by the environment or scenario (e.g., loss of satellite signals due to urban canyon or bad image quality). The main localization modes for the automotive application are therefore generated here depending on the available GNSS information. This block is composed of:

- **An error state Extended Kalman filter (EKF)** as main estimator that combines the GNSS and INS measurements in a tightly coupled fashion to provide position, velocity and other related estimated magnitudes. Different EKF filter running in parallel with different hypothesis subsets of measurements can be considered in the future to allow for a solution separation fault detection and integrity quantification.
- **Fault detection and Exclusion (FDE)** functions that targets those faults that were not detected on the Local threats protection block. The relevant possible faults are considered within a threat model that is described later. Both a solution separation and an innovation-based fault detection are considered.
- **Integrity Monitoring** block which is the main responsible for computing the protection levels based on the EKFs estimator and the fault detection information.

The IMU measurements (i.e., specific forces and angular rates) are processed by a strapdown computer in order to obtain the Inertial Navigation System (INS) magnitudes attitude, position and velocity over time. The solution of the INS is the main positioning solution provided by the INS channel. In order to prevent the estimated pose from drifting over time due to the IMU error processes, an error state Extended Kalman filter is implemented to calibrate the INS system over time thanks to GNSS or other information. An error state version of the EKF is chosen so that effects due to linearization of the INS differential equations does not have a significant impact on the representations of the error estimation provided by the filter. Since the main purpose of the EKF is to estimate the errors in the INS system, the EKF will always contain the following INS related states $\mathbf{x}_{\text{INS}}$:

$$\mathbf{x}_{\text{INS}} = \begin{pmatrix} \delta\boldsymbol{\psi}^T & \delta\mathbf{v}^T & \delta\mathbf{p}^T & \mathbf{b}_f^T & \mathbf{b}_w^T \end{pmatrix}^T \tag{7}$$

where $\delta\boldsymbol{\psi}$, $\delta\mathbf{v}$ and $\delta\mathbf{p}$ are the 3D error in attitude, velocity and position of the INS system respectively. This leads to the classical 15 main states of the filter. Depending on the characteristics of the IMU under used, the filter may consider additional 3D accelerometer scale factors and 3D gyroscope scale factors and/or misalignment quantities. The implementation of this part of the filter is well known in the community (Groves, 2013). A very important aspect is the correct error modelling of the inertial sensor errors. This must be carefully performed offline typically by using different calibration procedures and error modelling tools like Allan variance. Deterministic errors are here assumed to be compensated for by the manufacturer or by a dedicated procedure before the run-time application so that they can be correctly parametrized. The remaining stochastic and time-correlated errors are estimated over time as bias states within the filter. When necessary and depending on the specific error behavior of the IMU axis measurements, more than one bias per axis could be considered to guarantee a trustable and accurate estimation. The bias terms are modelled as first order Gauss-Markov processes with the parameters determined (and possibly parametrized) from for instance Allan variance analysis (IEEE, 1998).

GNSS is used in differential RTK mode, therefore, it is necessary to consider additional states. The additional GNSS related states that are included in the EKF are related to the float single difference ambiguities $\mathbf{N}$:

$$\mathbf{x}_{\text{GNSS}} = \begin{bmatrix} \mathbf{N}_{\text{G}}^{f1} & \mathbf{N}_{\text{G}}^{f2} & \mathbf{N}_{\text{E}}^{f1} & \mathbf{N}_{\text{E}}^{f2} \end{bmatrix}^T \tag{8}$$

where the subscript indicates the constellation and the superscript the satellite signal frequency. In the following, we only solve for the float solution, so no ambiguity fixing technique is applied.

At the moment, we are considering short baselines (i.e., baselines below $20\,\mathrm{km}$). Hence, we assume the tropospheric and ionospheric propagation delays to be equivalent at the reference station and the rover. Longer baselines could be also considered by additionally model the tropospheric and ionospheric delay differences within the filter.

The measurement model is based on the double-difference (DD) pseudorange and phase measurements. According to (Groves, 2013), these measurements for satellite s given the reference satellite t are be expressed as

$$\nabla\Delta\tilde{\rho}^{ts}_{\text{GNSS}} = \tilde{\rho}^{s}_{r} - \tilde{\rho}^{t}_{r} - \left(\tilde{\rho}^{s}_{b} - \tilde{\rho}^{t}_{b}\right), \tag{9}$$

$$\approx (\mathbf{u}^{s}_{r} - \mathbf{u}^{t}_{r})\mathbf{x}_{r,b} + \nabla\Delta\epsilon_{\rho}, \tag{10}$$

$$\nabla\Delta\tilde{\Phi}^{ts}_{\text{GNSS}} = \tilde{\Phi}^{s}_{r} - \tilde{\Phi}^{t}_{r} - \left(\tilde{\Phi}^{s}_{b} - \tilde{\Phi}^{t}_{b}\right), \tag{11}$$

$$\approx (\mathbf{u}^{s}_{r} - \mathbf{u}^{t}_{r})\mathbf{x}_{r,b} + \lambda(\Delta N_s - \Delta N_t) + \nabla\Delta\epsilon_{\Phi}, \tag{12}$$

where $\tilde{\rho}^{i}_{r}$ and $\tilde{\Phi}^{i}_{r}$ denote the pseudorange and phase measurement of the i satellite at the rover, whereas the subscript b indicates the same for the reference base station. The reference satellite t is chosen to be the one with the highest elevation angle. The single difference ambiguities for satellite s are denoted by $\Delta N_s = N^{r}_{s} - N^{b}_{s}$ and λ is the wavelength of the satellite signal. The quantities $\nabla\Delta\epsilon_{\rho}$ and $\nabla\Delta\epsilon_{\Phi}$ describing the remaining double difference multipath and noise component for pseudorange and phase measurements, respectively. The line of sight vector for each satellite i at the rover is expressed by $\mathbf{u}^{i}_{r}$.

For the EKF measurement model, we compute the difference between GNSS measurement based DD and expected DD based on the position of the calibrated INS and obtained satellite positions:

$$z = \begin{bmatrix} \nabla\Delta\tilde{\rho}^{ts}_{\text{GNSS}} - \nabla\Delta\hat{\rho}^{ts}_{\text{INS}} \\ \nabla\Delta\tilde{\Phi}^{ts}_{\text{GNSS}} - \nabla\Delta\hat{\rho}^{ts}_{\text{INS}} \end{bmatrix}. \tag{13}$$

For the corresponding measurement covariance matrix $\mathbf{R}$, we assume in this work the same satellite elevation depending pseudorange noise model all constellations and frequencies, similar the phase noise model:

$$\sigma^{i}_{\rho} = \frac{\sigma_{\rho}}{\sqrt{\sin el_i}}, \qquad \sigma^{i}_{\Phi} = \frac{\sigma_{\Phi}}{\sqrt{\sin el_i}}.$$

Hence, we can express the measurement covariance matrix as block diagonal matrix with the off-diagonal elements are zero and diagonal matrices:

$$\mathbf{R} = \text{blkdiag}\left(\mathbf{R}^{f_1}_{G,\rho}, \mathbf{R}^{f_2}_{G,\rho}, \mathbf{R}^{f_1}_{E,\rho}, \mathbf{R}^{f_2}_{E,\rho}, \mathbf{R}^{f_1}_{G,\Phi}, \mathbf{R}^{f_2}_{G,\Phi}, \mathbf{R}^{f_1}_{E,\Phi}, \mathbf{R}^{f_2}_{E,\Phi}\right) \tag{14}$$

where the constellation-frequency dependent pseudorange covariance matrices are given by

$$\mathbf{R}^{f}_{c,\rho} = \text{DD}^{f}_{c,\rho}\mathbf{\Sigma}^{f}_{c,\rho}{\text{DD}^{f}_{c,\rho}}^{T}, \tag{15}$$

where each signal covariance matrix $\mathbf{\Sigma}^{f}_{c,\rho}$ is a diagonal matrix with σ^2_{ρ} as diagonal elements and zeros as off-diagonal elements. The same applies for the phase covariance matrices $\mathbf{R}^{f}_{c,\Phi}$. The double difference matrix $\text{DD}^{w,t}_{c}$ for constellation c, signal frequency f and reference satellite t has a size of $(L_{c,f} - 1) \times L_{c,f}$, and the number of available satellites per constellation and frequency is denoted by $L_{c,f}$. The double difference matrix, if the first available satellite is chosen as reference satellite, is given by:

$$\text{DD}^{f,t}_{c} = \begin{bmatrix} -1 & 1 & 0 & \dots & 0 \\ -1 & 0 & 1 & \dots & 0 \\ \vdots & \vdots & \vdots & \ddots & \vdots \\ -1 & 0 & 0 & \dots & 1 \end{bmatrix} \tag{16}$$

For simplicity, we omit the superscript t for the reference satellite.

Finally, when static periods of time are detected, the filter performs Zero Velocity Updates and Zero Angular Rate Updates that aid in the initial convergence of the filter, in estimating the inertial sensor biases and in preventing a high drift of the heading error until the vehicle starts or resumes movement.

3. OBU Integrity Monitoring

Based on the nominal error models used for the Kalman filter, the threat model, the test statistics defined in the previous section and the required integrity risk (IR), a protection level (PL) is computed. In this work the protection level is ultimately based on a normalized innovation square fault detection, which assumes the presence of a residual single fault. This assumption is made based on the expected performance of the batch of local threats detectors and logic that are introduced per channel before GNSS measurements reach the KF and the expected performance of the innovation screening detector, which discard any measurement suspected of not belonging to the nominal error model. This conclusion is validated based on the analysed data in the result section with Figure 10. For the local test statistics, we analyze each of the innovation vector elements related to each of the visible ground stations independently. This is commonly referred to as innovation screening. The normalized innovation for the element j serves as our local test statistic (García Crespillo et al., 2017a):

$$q_k^j = \frac{\boldsymbol{\gamma}_k^j}{\sqrt{\left[\mathbf{S}_k^{-1}\right]_{jj}}} \tag{17}$$

since the innovation vector follows a Gaussian distribution, so does the local test statistic. In the nominal case (H_0 hypothesis), each of the local tests follows a standard normal distribution, in case of a faulty measurement (H_1 hypothesis) the corresponding distribution is biased:

$$\text{H0: } q_k^j \sim \mathcal{N}(0,1) \tag{18}$$

$$\text{H1: } q_k^j \sim \mathcal{N}(\mu_j,1) \tag{19}$$

Given a certain probability of false alarm $P_{\text{fa, IS}}$, a suitable threshold can be found by means of the inverse Normal distribution. In case the normalized innovation is above this threshold, the corresponding measurement is excluded from the EKF measurement update step. All innovations passing the innovation screening step are further considered.

For the second local test that is ultimately used to support the protection level computation, we investigate the sum of normalized innovation squares related to each of the visible ground stations independently. This is commonly referred to as Normalized Innovation Square (NIS) local test statistic (Grosch et al., 2017).

This test statistic $q_{\text{NIS},k}$ is obtained by:

$$q_{\text{NIS},k} = \boldsymbol{\gamma}_k^T \mathbf{S}_k^{-1} \boldsymbol{\gamma}_k. \tag{20}$$

In the GNSS fault-free case H0, i.e., no local threats are present, this test statistic is assumed to follow a chi-square distribution with L degrees of freedom. In the faulty case, the test statistic is following a non-central chi-square distribution with L degrees of freedom and non-central parameter

$$\lambda_m = \boldsymbol{\mu}_\gamma^T \boldsymbol{\mu}_\gamma, \tag{21}$$

where $\boldsymbol{\mu}_\gamma$ represents the bias on each innovation caused by the measurement fault. We can state:

$$\text{H0} : q_{\text{NIS},k} \sim \chi^2(L) \tag{22}$$

$$\text{H1} : q_{\text{NIS},k} \sim \chi^2(L, \lambda_m). \tag{23}$$

The detection threshold is found by using the inverse chi square cumulative density function for L degrees of freedom and a maximum allowed probability of false alarm $P_{\text{fa, NIS}}$. The latter is retrieved from the availability and continuity system requirement. If the test statistic exceeds the corresponding threshold, a fault is triggered.

If the test is passed, we assume the innovation to be consistent and compute the protection level. As we proposed in (García Crespillo et al., 2017b), we compute the horizontal protection level as

$$HPL = Hslope_{max} \sqrt{T(L, P_{\text{fa, NIS}})} + K_{ff} \sqrt{P_{ee} + P_{nn}}, \tag{24}$$

where P_{ee} and P_{nn} are the covariance diagonal elements addressing the estimated east and north position error uncertainty and K_{ff} an inflation factor corresponding to the allowed probability of missed detection. Under non-nominal conditions, the presence of a fault projects both on the estimated position error and the test statistic. The relation between how much in each

part is affected is known as the slope. A bigger slope brings us faster to the integrity risk area. The protection levels are here computed by assuming the maximum (worst-case) slope for a single satellite fault hypothesis. For a certain fault vector $\mathbf{f}$, the horizontal slope under single fault assumption can be expressed as:

$$Hslope_{\gamma,k,i} = \sqrt{\frac{\mathbf{f}_i^T \mathbf{K}_k^T \boldsymbol{\epsilon}_n^T \boldsymbol{\epsilon}_n \mathbf{K}_k \mathbf{f}_i + \mathbf{f}_i^T \mathbf{K}_k^T \boldsymbol{\epsilon}_e^T \boldsymbol{\epsilon}_e \mathbf{K}_k \mathbf{f}_i}{\mathbf{f}_i^T \mathbf{S}_k^{-1} \mathbf{f}_i}} \tag{25}$$

where ϵ selects the desired state from the full state vector, $\mathbf{K}_k$ is the current time Kalman gain and $\mathbf{S}_k$ is the covariance associated with the current time innovation vector. Being the vector $\mathbf{f}_i$ a vector containing zeros except for the corresponding satellite position under evaluation.

4. Camera Processing

The camera processing block provides additional capability to the onboard unit to improve the overall availability and accuracy of the system. In specific urban environments such as in urban canyons or tunnels, the onboard navigation system may experience a relatively long period of time without reliable reception of GNSS signals. In such challenging scenarios, since the error from IMU will accumulate over time, the availability of GNSS/INS based navigation may degrade given that the integrity of the system must be guaranteed. The vision system will play a significant role in such cases to localize the vehicle and to keep it staying in the correct lane. As in our test set-up, it is assumed that two front-facing cameras are mounted on left and right side of the car respectively so that a well-aligned stereo rig can be formed. The triggering clocks of both cameras needs to be synchronized, e.g., using Precise-Time-Protocol (PTP), etc. The left and right cameras must be calibrated before utilization, so that the camera intrinsic parameters and the extrinsic parameters between the two cameras are estimated in a controlled environment. The uncertainty of the calibrated parameters are taken into consideration and are propagated into the localization uncertainty in the onboard processing. The procedure of the camera processing is shown in Fig. 4. The processing starts when

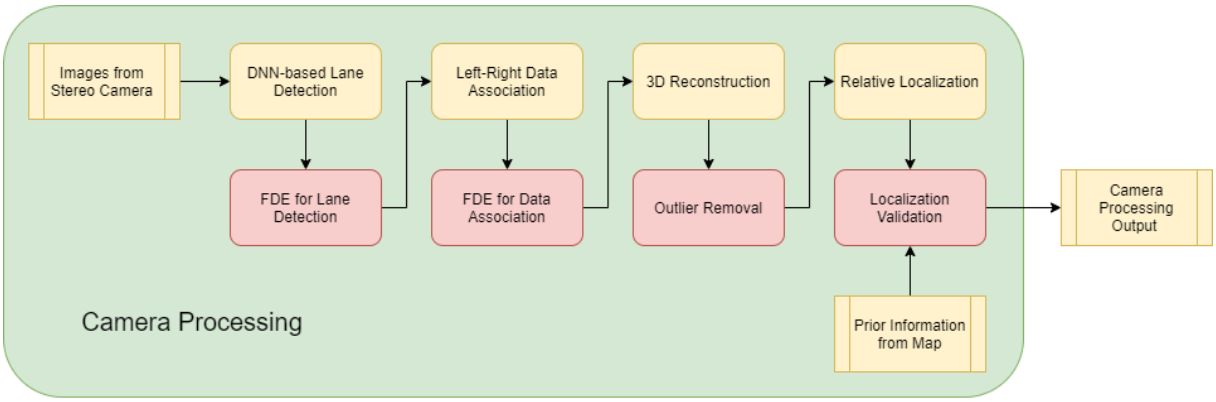

Figure 4: Onboard Camera Processing Module

both measurement images from the stereo rig are available. A Deep Neural Network (DNN) based lane detector is applied on both left and right images independently, exploiting its outstanding detection performance in challenging real-life scenarios, especially when occlusions and curved lane markers appear in the scenes. The applied neural network is a modified version of the SCNN (Spatial Convolutional Neural Network) for lane marker segmentation proposed by Pan et al. (2018). The SCNN assigns each pixel in the input image with a binary label, which indicates whether it belongs to a lane marker or not, and it supports multiple different lane segments (4 as default) distinguished by the output channels. Then the same lane marker in the left and right images are associated according to the projective geometry between the two cameras and the ground plane. The details of the DNN based lane detection as well as the data association and their error analysis can be found in the publication (Hao et al., 2021). With the aligned image points in both views, the 3D location of the lane markers can be reconstructed, and as a result, the relative distance from the vehicle (in the vehicle's body frame) to both closest lanes on both sides can be estimated.

The central role of safety and reliability is a distinguished aspect of our camera processing module design. It can be seen from the block diagram in Fig. 4 that a fault detection and elimination (FDE) function block is added after each step of processing (marked as red blocks). The design of the FDE functions follows the multi-domain error monitoring concept proposed for visual navigation integrity by Zhu et al. (2022). The neural network outputs are first independently denoised and validated according to projective geometry. Then, the associated data is tested according to the nominal error distribution. Similar method as from Zhu et al. (2020) can be applied if a quantified association failure probability is required. Points with large 3D position error can still exist after 3D reconstruction, so an outlier removal is essential before localizing the vehicle to the lane markers. As a

last safety checking, the prior information of the lane width is applied to validate the calculated distance to the borders of the lane. Only if all the FDE tests are passed, the camera processing block outputs the relative localization information including the camera measurements timestamps, the flag of the processing (successful or not), the estimated distance to the lane markers, and the reliability metrics of the output to the mode selector.

In our demonstration campaign in Rome, an example of the camera based lane detection and in-lane localization results is shown in Fig. 5.

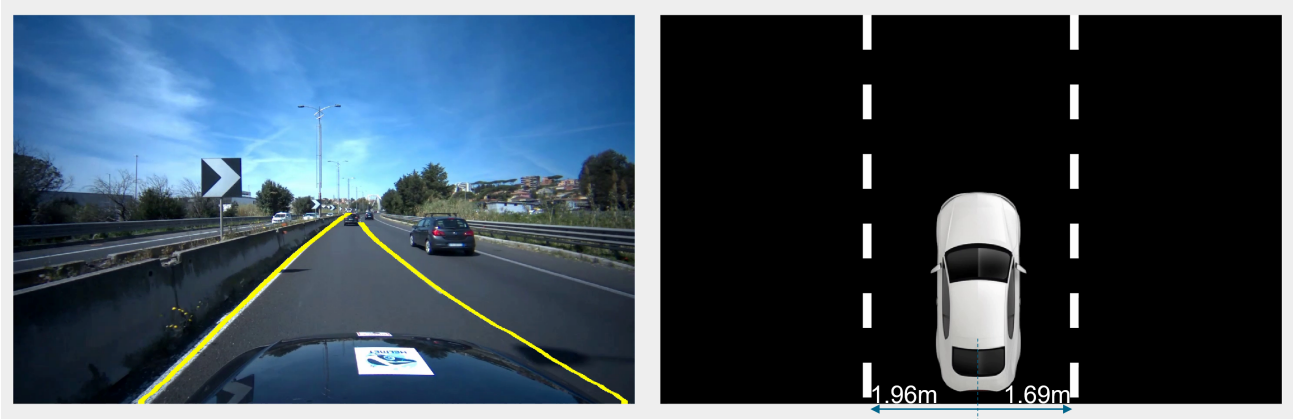

Figure 5: Camera Lane Detection and In-lane Localization

5. Localization Mode Selector

The localization mode selector function acts as a user interface by providing the best solution available from the different sensors and systems. It is here assumed that the main INS filter and integrity monitoring provides the most complete and risk quantifiable information of the position of the vehicle. There may be however situations when the protection levels might exceed a certain level that is unacceptable by the current operational scenario or necessary information are not available such as AIMN data link. This block may decide that it is better to provide at least partial solution (e.g., only lateral) coming from the relative positioning based on the camera system.

V. EXPERIMENTAL SETUP AND TEST CAMPAIGN

1. Hardware Equipment

For the HELMET validation, the following three GRDNet Reference Stations have been used for the implementation of the 2-Tiers algorithm for the validation area (Roma-Fiumicino area in the centre of Italy): RIET, ROMA and TERN. The map, showing the geographical distribution of the second tier Reference Station, are shown in Fig. 6a.

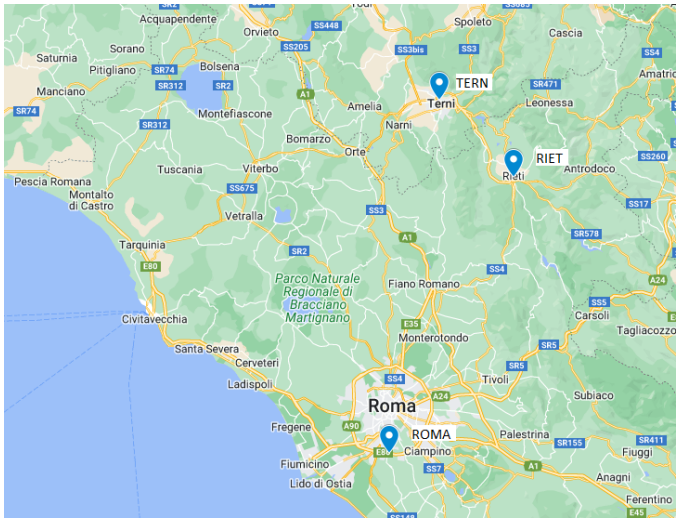

(a) Used 2-tier AIMN Reference Station and their locations

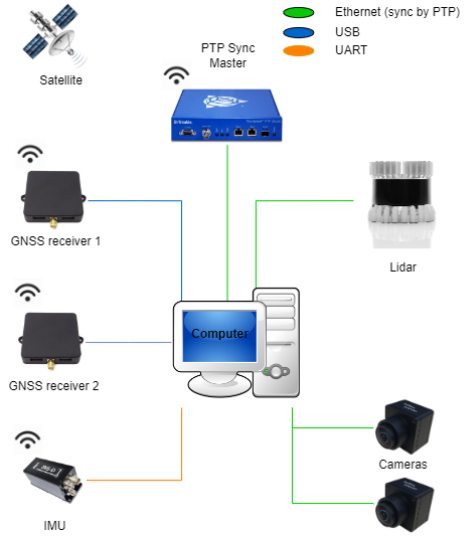

(b) Onboard Experimental Sensor Setup and connections

Figure 6: Setup for Demo Campaign in Rome, Italy

The onboard equipment is shown in Figure 6b and consists of two Septentrio Mosaic GNSS receivers with multi-band antennas, Inertial Labs INS-D, a pair of global-shutter cameras Triton 2.3 from Lucid Vision, Ouster lidar, Trimble PTP GM200 for clock synchronisation, and a central computing unit to mange the sensor system, provide connectivity, and to record sensor data. A key enabler of the onboard unit is the clock synchronisation of individual components, which has been achieved by utilising GNSS system time to discipline GNSS receivers, inertial unit, and Precise-Time-Protocol (PTP) source. The PTP synchronizes over the Ethernet both cameras and lidar. The onboard unit records timestamped sensor data streams, which have been used for the post-processing.

(a) Placement of stereo camera, inertial sensor and LIDAR.

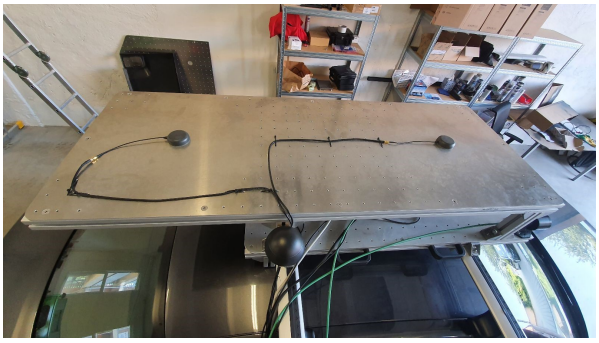

(b) Placement of Dual Frequency, Dual Constellation GNSS antennas on top.

Figure 7: OBU Hardware setup.

2. Test Campaign

The test campaign the results in this paper are based on was performed on April 12, 2022 in Rome, Italy. The setup comprised a ground vehicle on which two GNSS antennas where mounted, one in front and one at the back as shown in Figure 7a and Figure 7b. An inertial measurement unit was also mounted to record inertial data and a calibrated camera to record videos during the entire campaign. The vehicle was setup in the vicinity of a base station that was installed prior to the start of the campaign to provide augmentation data through RTCM messages.

The measurement campaign consisted of a start with a static period of time in a yard in an urban area. This static period was shortly followed by a series of turn manoeuvres. The vehicle was then driven from the urban area towards a highway, through some tunnels for a few minutes then returned to the start point of the campaign The trajectory of the vehicle is shown in Fig. 8 and the available GPS and Galileo satellites are indicated via a skyplot in Fig. 9.

For the configuration of the RTK/INS filter and integrity monitoring the parameters in Table 1 were used.

System Parameters	Values
Initial state uncertainty SD ambiguities	100
SD ambiguities state transition uncertainty	1×10^{-5}
Pseudorange measurement noise σ^i_ρ	$4\,\mathrm{m}$
Phase measurement noise σ^i_Φ	$0.01\,\mathrm{m}$
Probability of false alarm IS	1×10^{-2}
Probability of false alarm NIS	1×10^{-6}
Probability of missed detection NIS	1×10^{-8}

Table 1: System parameters

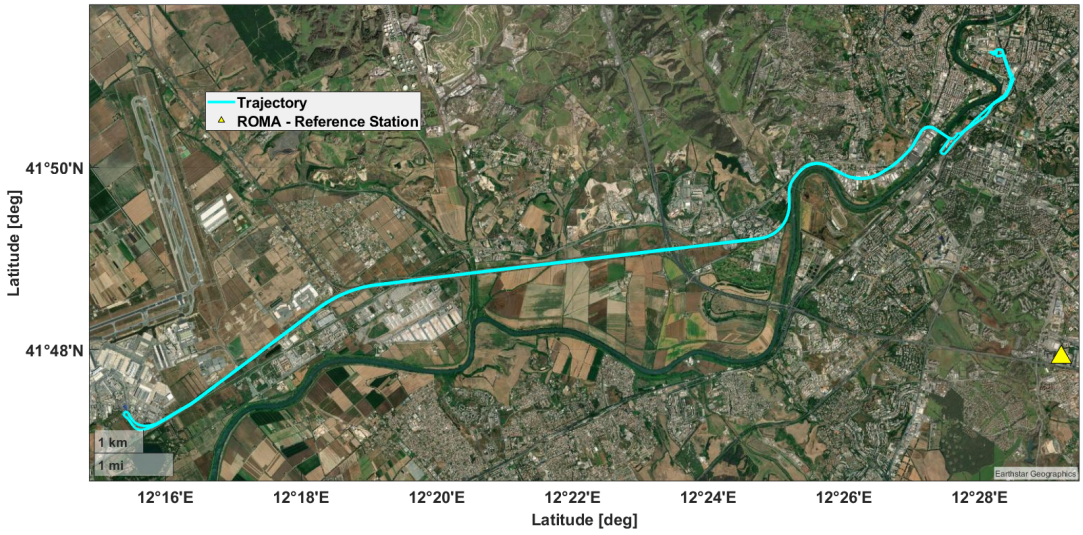

Figure 8: Trajectory including the location of the AIMN reference station ROMA.

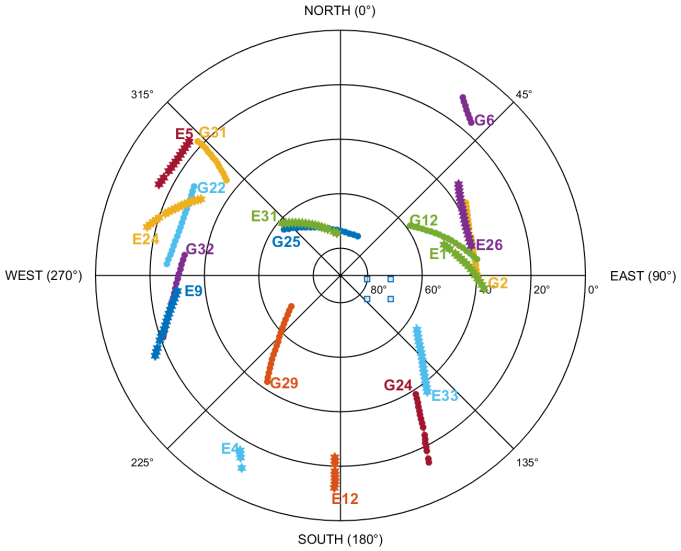

Figure 9: Skyplot of the received GPS (circular markers) and Galileo (hexagon markers) satellites after applying the local threat protection block.

VI. RESULTS

1. Minimizing the residual probability of local GNSS fault

Due to multi-layer GNSS fault detection and exclusion architecture, the remaining undetected GNSS faults are assumed to have a very low probability such that it is here leveraged to assume a single simultaneos satellite fault. To illustrate the impact of the usage of local threat protection and detection techniques on the remaining errors, we computed the folded cumulative density function of the normalized innovations over all satellite signals and all epochs after different stages. Figure 10a shows

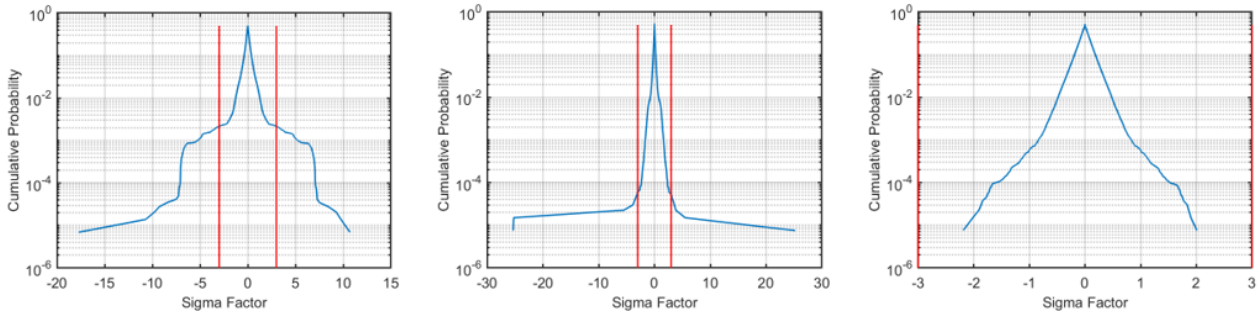

(a) Postcorrelation measurement residuals **(b)** After applying local FDE **(c)** After applying innovation screening

Figure 10: Cumulative probability of normalized KF residuals of measurements at different processing stages

the folded cumulative probability distribution of the normalized KF residuals of code and phase measurements as they are provided by the receiver after correlation. The two red lines marked a 3 sigma threshold, which is here used as a criteria to classify a measurement as faulty. As we can see, in Figure 10a, there is substantial probability mass that extends beyond the threshold, indicating ultimately tha the probability of simultaneous faults is highly frequent (as expected in urban environments). Figure 10b depicts the same distribution when several local threats protection and logic are applied. In this case, it was considered a Carrier-To-Noise masks, a cycle slip detector and a multipath detector based on CMCD. As we can see, the probability mass concentrates much more inside the thresholds but there exists still long tails that accumulates probabilities higher than 1E-5. Finally, Figure 10c considers the cumulative probability of the measurement KF residuals considering the local threats blocks and an innovation screening. We can see that all the probability mass (given the avaialble measurements over the experimental tests) stays below the 3 sigma threshold. Given the number of available measurements we can assume that the residual probability of fault after the protections may be below 1E-5, which is here used to make the assumption of single simultaneous fault and can be used in the future as an input for a solution separation integrity monitoring algorithm.

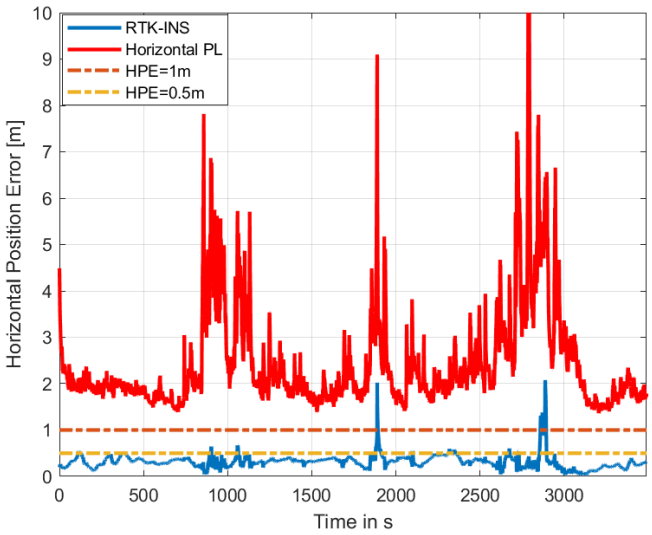

(a) Horizontal Position Error (HPE) and Horizontal Protection Level including constant performance identifier of one meter and half a meter horizontal position error.

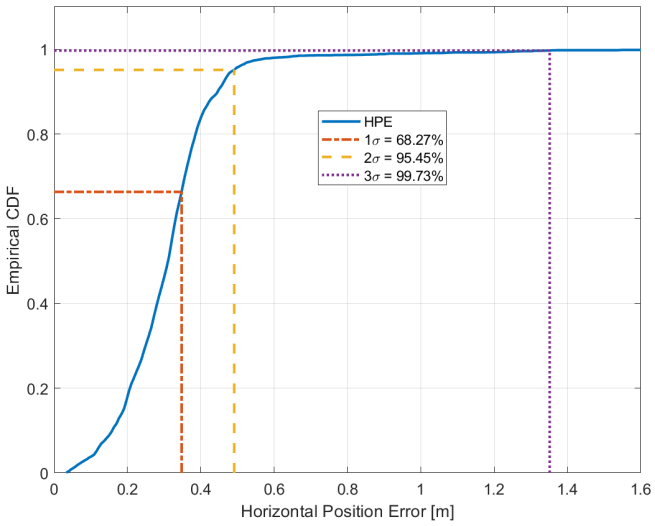

(b) Empirical cumulative density function of obtained horizontal position error including the accuracy quantile of $68.27\,\%$ = $34.76\,\mathrm{cm}$, $95.45\,\%$ = $49.10\,\mathrm{cm}$ and $99.73\,\%$ = $135.16\,\mathrm{cm}$

Figure 11: Horizontal protection level and position error results.

2. Position Accuracy and Protection Level

Fig. 11a shows the horizontal position error (HPE) as well horizontal protection level (HPL) over the whole demo run. For better comparison, we have also included two performance lines, i.e. half a meter HPE and one meter HPE. As it can be seen, the obtained HPE is below or equal to half a meter in $95.5\,\%$ and below or equal to one meter in $99.05\,\%$ of the cases. For a more detailed analyse, we provide the empirical cumulative density plot of the HPE in Fig. 11b. The plot depicts that the accuracy quantile of $68.27\,\%$ is equal to a HPE of $34.76\,\mathrm{cm}$, $95.45\,\%$ is equal to a HPE of $49.10\,\mathrm{cm}$ and $99.73\,\%$ is equal to a HPE of $135.16\,\mathrm{cm}$.

VII. DISCUSSIONS

Due to multi-layer GNSS fault detection and exclusion architecture, the remaining undetected GNSS faults are assumed to be one a single satellite. This assumption might be conservative but reasonable. The lower half Standford in Fig. 12a analyze the obtained integrity results. That is the horizontal axis is the Horizontal Position Error (HPE) and the vertical axis the Horizontal Protection Level (HPL). Each bin indicates the number of occurrences of a specific (HPE,HPL) pair. Any pair laying the white area represents a true overbound of our solution, whereas any pair laying in red triangle would represent misleading information, i.e., the protection level does not overbound the position error. As it can be seen, our observed HPL-HPE pairs lay only in the white area. However, the protection level is often much bigger than the corresponding HPE, hence we might be to conservative in some cases. Depending on the required mode of operation, and therefore, resulting required alert limit, this might lead to increased but unnecessary system unavailability. Since the system is set unavailable as soon as the protection level excesses the alert limit. For instance, a horizontal alert limit of four meter would cause a system unavailability in $8.86\,\%$ while the actual horizontal position error in always below $2.1\,\mathrm{m}$.

The empirical cumulative density function of the obtained horizontal protection level can be seen in Figure 12b. As you can see protection level under one and a half meters are only observed in four percent of the cases, below two meters for $54\,\%$ and below three meters for $83\,\%$, respectively. Depending on the mode of operation these results might violate the corresponding horizontal alert limit requirement and lead to a decrease of system availability Remember this protection levels are based on a single fault assumption. Therefore, we want to exploit Kalman filter based solution separation techniques. So, we consider different fault modes such as RTK reference satellite faults and carefully revise the budget allocation. All this might lead also lead to lower protection levels and higher system availability.

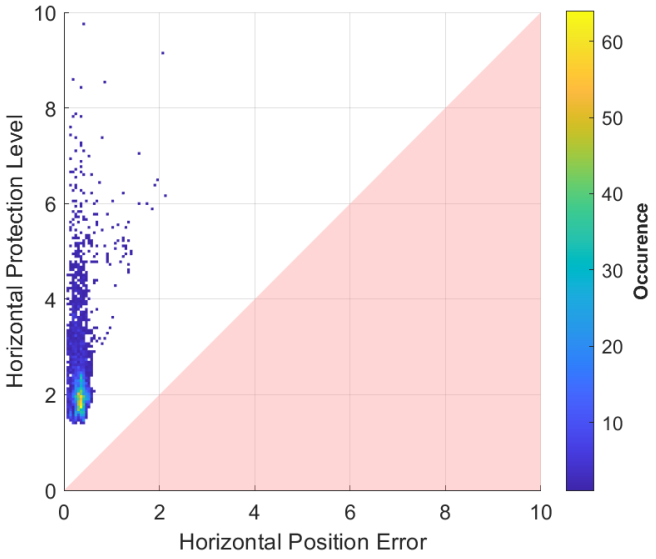

(a) Lower half Stanford plot: The horizontal axis is the Horizontal Position Error (HPE) and the vertical axis the Horizontal Protection Level (HPL). Each bin indicates the number of occurrences of a specific (HPE,HPL) pair.

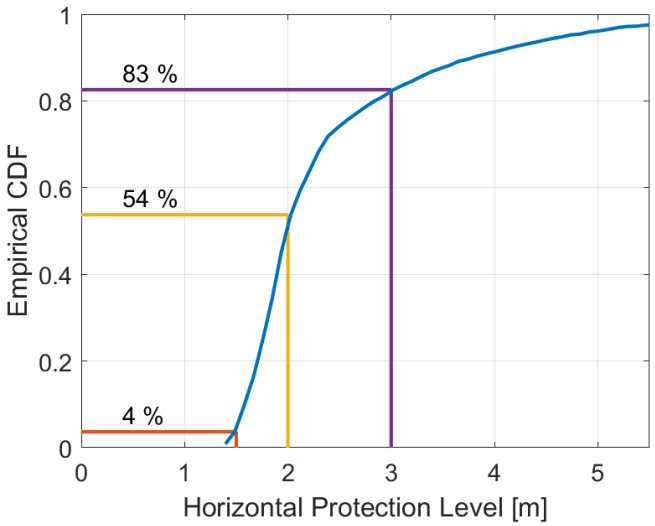

(b) Empirical cumulative density function of obtained horizontal protection levels including identification of HPL being small or equal to one and a half, two and three meters, respectively.

Figure 12: Evaluation of obtained Horizontal Protection Levels.

VIII. CONCLUSIONS

Ensuring high accuracy and high integrity positioning is necessary for new emerging applications. It is however, very challenging to satisfy rigorously both simultaneously. The use of carrier-phase based positioning is indispensable in combination with additional sensors. The general architecture proposed in this work could be a good candidate starting point for achieving these requirements. Further investigations about the fault probabilities, not only of residual local threats but also of the additional sensors will be carried in the future. Although relatively low protections levels were obtained, achieving even tighter protection levels might require fixing the ambiguities, for which a rigorous integrity assessment needs to be still considered. The proposed architecture and aspects discussed in this paper may not only be considered as a baseline for automotive but also for other applications in challenging GNSS environments.

ACKNOWLEDGEMENTS

This work has received funding from the European Union's Horizon 2020 research and innovation programme under Grant Agreement No: 870257 HELMET project.

REFERENCES

Bijjahalli, S. and Sabatini, R. (2021). A high-integrity and low-cost navigation system for autonomous vehicles. *IEEE Transactions on Intelligent Transportation Systems*, 22(1):356–369.

Bryant, R., Julien, O., Hide, C., Schuerch, C., and Sheret, I. (2019). Mass market lane accurate positioning with high integrity. In *Proceedings of the 32nd International Technical Meeting of the Satellite Division of The Institute of Navigation (ION GNSS+ 2019)*, pages 573–593, Miami, Florida.

Caamano, M., Crespillo, O. G., Gerbeth, D., and Grosch, A. (2020). Detection of gnss multipath with time-differenced code-minus-carrier for land-based applications. In *European Navigation Conference 2020 (ENC 2020)*.

Garcia Crespillo, O., Gerbeth, D., Sabina, S., Cascallana, R., Coluccia, A., Aguila, A., Barre, A., Peinado, J., and Marais, J. (2019). Ersat ggc. ertms on satellite galileo game changer: Deliverable d4.5 - process execution report.

García Crespillo, O., Grosch, A., and Meurer, M. (2017a). Detection of DME Ranging Faults with INS Coupling. In *2017 Integrated Communication, Navigation and Surveillance Conference (ICNS)*.

García Crespillo, O., Grosch, A., Skaloud, J., and Meurer, M. (2017b). Innovation vs Residual KF Based GNSS/INS Autonomous Integrity Monitoring in Single Fault Scenario. In *ION GNSS+ 2017*, Portland, OR, USA.

Grosch, A., Crespillo, O. G., Martini, I., and Günther, C. (2017). Snapshot residual and kalman filter based fault detection and exclusion schemes for robust railway navigation. In *2017 European Navigation Conference (ENC)*, pages 36–47.

Groves, P. D. (2013). *Principles of GNSS, Inertial, and Multisensor Integrated Navigation Systems*. Artech House, second edition.

GSA (2019a). Report on Aviation User Needs and Requirements. Technical Report GSA-MKD-AV-UREQ-250287, European Global Navigation Satellite System Agency.

GSA (2019b). Report on Rail User Needs and Requirements. Technical Report GSA-MKD-RL-UREQ-250286, European Global Navigation Satellite System Agency.

GSA (2019c). Report on Road User Needs and Requirements. Technical Report GSA-MKD-RD-UREQ-250283, European Global Navigation Satellite System Agency.

Hao, W., Zhu, C., Garcia Crespillo, O., and Meurer, M. (2021). Error assessment of deep learning based lane detection. In *Navigation 2021 (The European Navigation Conference (ENC) & The International Navigation Conference (INC))*.

IEEE (1998). IEEE standard specification format guide and test procedure for single-axis interferometric fiber optic gyros. Technical report.

Joerger, M. and Spenko, M. (2017). Towards navigation safety for autonomous cars. *Inside GNSS*.

Meng, Q. and Hsu, L.-T. (2021). Integrity monitoring for all-source navigation enhanced by kalman filter-based solution separation. *IEEE Sensors Journal*, 21(14):15469–15484.

Neri, A., Capua, R., and Salvatori, P. (2015). High integrity two-tiers augmentation systems for train control systems. In *2015 Proceedings of the ION 2015 Pacific PNT Meeting, Honolulu*.

Pan, X., Shi, J., Luo, P., Wang, X., and Tang, X. (2018). Spatial as deep: Spatial cnn for traffic scene understanding. In *Thirty-Second AAAI Conference on Artificial Intelligence*.

Reid, T. G., Houts, S. E., Cammarata, R., Mills, G., Agarwal, S., Vora, A., and Pandey, G. (2019). Localization requirements for autonomous vehicles. *SAE International Journal of Connected and Automated Vehicles*, 2(3).

Saidani, M., Maya, D. G., and Guinamard, A. (2021). High integrity multi-sensor navigation system for safety critical applications. In *Proceedings of the 34th International Technical Meeting of the Satellite Division of The Institute of Navigation (ION GNSS+ 2021)*.

Toledo-Moreo, R., Zamora-Izquierdo, M. A., Ubeda-Minarro, B., and Gomez-Skarmeta, A. F. (2007). High-integrity imm-ekf-based road vehicle navigation with low-cost gps/sbas/ins. *IEEE Transactions on Intelligent Transportation Systems*, 8(3):491–511.

Vennarini, A., Coluccia, A., Gerbeth, D., Crespillo, O. G., and Neri, A. (2020). Detection of gnss interference in safety critical railway applications using commercial receivers. In *Proceedings of the 33rd International Technical Meeting of the Satellite Division of The Institute of Navigation (ION GNSS+ 2020)*, pages 1476–1489.

Zhu, C., Joerger, M., and Meurer, M. (2020). Quantifying feature association error in camera-based positioning. In *2020 IEEE/ION Position, Location and Navigation Symposium (PLANS)*, pages 967–972, Portland, OR, USA. IEEE/ION, IEEE.

Zhu, C., Meurer, M., and Günther, C. (2022). Integrity of visual navigation—developments, challenges, and prospects. *NAVIGATION: Journal of the Institute of Navigation*, 69(2).

Zhu, N., Marais, J., Bétaille, D., and Berbineau, M. (2018). Gnss position integrity in urban environments: A review of literature. *IEEE Transactions on Intelligent Transportation Systems*, 19(9):2762–2778.